

Figure 19.3b on page 591 is reprinted from “Galaxies in the Young Universe,” by F. Duccio Macchetto and Mark Dickinson, © 1997 by Scientific American, Inc. All rights reserved.

Astronomy and Astrophysics Library
Malcolm S. Longair, **Galaxy Formation**, 2nd ed.
© 2008 Springer-Verlag Berlin Heidelberg

In this chapter, we summarise the results of programmes to determine the cosmological parameters discussed in Chap. 7 by the observation of distant objects, such as galaxies, clusters of galaxies and quasars. The information which can be derived from observations of the Cosmic Microwave Background Radiation and the large-scale distribution of galaxies will be described in Chap. 15, once the tools necessary to interpret these data have been developed. Therefore, the discussion presented in this chapter is necessarily incomplete. All the information will be synthesised into a consistent picture, what is often referred to as the *concordance model*, in Sect. 15.9.

8.1 The Cosmological Parameters

We can summarise the results of the calculations of Chap. 7 for observational cosmology as follows. The standard uniform world models can be described by a small number of parameters:

- *Hubble’s constant*, H_0 , describes the present rate of expansion of the Universe,
- The *deceleration parameter*, q_0 , describes the present dimensionless deceleration of the Universe

$$H_0 = \left(\frac{\dot{a}}{a} \right)_{t_0} = \dot{a}(t_0). \quad (8.1)$$

$$q_0 = - \left(\frac{\ddot{a}a}{\dot{a}^2} \right)_{t_0} = - \frac{\ddot{a}(t_0)}{H_0^2}. \quad (8.2)$$

- The *density parameter* Ω_0 , is defined to be the ratio of the present mass-energy density of the Universe ϱ_0 to the critical density $\varrho_c = 3H_0^2/8\pi G$,

$$\Omega_0 = \frac{\varrho_0}{\varrho_c} = \frac{8\pi G \varrho_0}{3H_0^2}. \quad (8.3)$$

For many aspects of astrophysical cosmology, it is important to determine separately the density parameter in baryonic matter Ω_B and the overall density parameter Ω_0 , which includes all forms of baryonic and non-baryonic dark matter.

- The density parameter of the vacuum fields, or the dark energy,

$$\Omega_\Lambda = 8\pi G \rho_\Lambda / 3H_0^2 = \Lambda / 3H_0^2, \quad (8.4)$$

where Λ is the cosmological constant.

- The curvature of space is given by $\kappa = c^2/\mathfrak{N}^2$.

- The age of the Universe T_0 is given by

$$T_0 = \int_0^1 \frac{da}{\dot{a}}. \quad (8.5)$$

As discussed in the Chap. 7, within the context of the Friedman world models, these are not independent parameters. Specifically, (7.51) and (7.62) show that

$$\kappa \left(\frac{c}{H_0} \right)^2 = (\Omega_0 + \Omega_\Lambda) - 1, \quad (8.6)$$

and

$$q_0 = \frac{\Omega_0}{2} - \Omega_\Lambda. \quad (8.7)$$

Other parameters will be introduced in Chap. 15 in relation to the formation of structure in the Universe.

The observational approach to the determination of these parameters can be appreciated from the relations presented in Sect. 7.4, specifically, Figs. 7.6 to 7.9 and 7.11. The basic point is that the variation of the different distance measures with redshift are determined by the dynamics and geometry of the Universe. Thus, if precise measurements of any of these relations could be made, the parameters Ω_0 and Ω_Λ could be estimated directly. The best approach would be to estimate precisely some distance measure, for example r , D , D_A or D_L , for some class of object by a technique which is *independent* of redshift and then plot the results on relations such as (7.6) or (7.7). This procedure is now possible in some of cosmological tests, as we will discuss.

A traditional approach has been to select objects which are believed to possess the same intrinsic properties at different redshifts and then determine how their observed properties vary with redshift; then, the angular diameter-redshift or flux density-redshift relations can be compared with the expectations of Figs. 7.8 and 7.9 respectively. This procedure is critically dependent upon our ability to identify reliably the same types of ‘standard candle’ or ‘rigid rod’ at different redshifts.

which are the basis of the standard models,

$$\dot{a} = -\frac{\Omega_0 H_0^2}{2a^2} + \Omega_\Lambda H_0^2 a^2 - \frac{c^2}{\mathfrak{N}^2}, \quad (8.8)$$

$$\ddot{a}^2 = \frac{\Omega_0 H_0^2}{a} + \Omega_\Lambda H_0^2 a^2 - \frac{c^2}{\mathfrak{N}^2}. \quad (8.9)$$

These equations describe two different aspects of the cosmological models. Equation (8.8) describes the deceleration, or acceleration, of the Universe under the competing influences of gravity and the dark energy. Expression (8.7) shows that the deceleration parameter provides a measure of the difference between half the density parameter Ω_0 and the density parameter in the vacuum fields Ω_Λ .

In contrast, (8.9) describes how the curvature of space, $\kappa = \mathfrak{N}^{-2}$, depends upon the total energy density in both the matter and the dark energy, as well as the kinetic energy of the expansion. The expression (8.9) describes the basic feature of the isotropic, homogeneous world models of General Relativity that the curvature of space at any epoch is determined by the total mass-energy density at any epoch. Furthermore, (5.32) shows that the space curvature changes as $\kappa = R_c^{-2}(t) = (\mathfrak{N}a)^{-2} \propto a^{-2}$, that is, its variation with cosmic epoch is independent of the details of the dynamics of the Universe. Let us look in a little more detail into how we can distinguish between these parameters observationally.

The deceleration of the Universe and its present mass density are separately measurable quantities. The density parameter Ω_0 can be found from the virial theorem in its various guises (Sect. 8.7). Inspection of the expressions for the comoving radial distance coordinate r and the distance measure D shows that the dynamical and geometrical properties of the models become entangled when we relate the intrinsic properties of objects at large redshifts to observables. It turns out, however, that at small redshifts the differences between the world models depend only upon the deceleration parameter and *not* upon the density parameter and the curvature of space. Let us demonstrate this by a simple argument given by Gunn (Gunn, 1978).

In order to relate observables to intrinsic properties, we need to know how the distance measure D depends upon redshift and this involved two steps. First, we worked out the dependence of the comoving radial distance coordinate r upon redshift z and then formed the distance measure $D = \mathfrak{N} \sin(r/\mathfrak{N})$. Let us first carry out this calculation in terms of the *kinematics* of a world model decelerating with deceleration parameter q_0 . We can write the variation of the scale factor a with cosmic epoch in terms of a Taylor series as follows:

$$\begin{aligned} a &= a(t_0) + \dot{a}(t_0) \Delta t + \frac{1}{2} \ddot{a}(t_0) (\Delta t)^2 + \dots \\ &= 1 - H_0 \tau - \frac{1}{2} q_0 H_0^2 \tau^2 + \dots, \end{aligned} \quad (8.10)$$

where we have introduced H_0 , q_0 and the look-back time $\tau = t_0 - t = -\Delta t$; t_0 is the present epoch and t is some earlier epoch. The above expansion can be written in terms of $x = H_0 \tau$ and so, since $a = (1+z)^{-1}$,

$$\frac{1}{1+z} = 1 - x - \frac{q_0}{2} x^2 + \dots. \quad (8.11)$$

8.2 Testing the Friedman Models

Let us first investigate in a little more detail the relation between the cosmological parameters and how we might disentangle them. To repeat the Einstein equations,

Now, we express the redshift z to second order in $x = H_0\tau$. This is achieved by making a further Taylor expansion of $[1 - x - (1/2)q_0x^2]^{-1}$ to second order in x . Carrying out this expansion, we find

$$z = x + \left(1 + \frac{q_0}{2}\right)x^2 + \dots \quad (8.12)$$

We can now find the expression for the comoving radial distance coordinate r by taking the integral

$$\begin{aligned} r &= \int_0^\tau \frac{c \, d\tau}{a} = \int_0^\tau c(1+z) \, d\tau \\ &= \frac{c}{H_0} \left[x + \frac{x^2}{2} + \left(1 + \frac{q_0}{2}\right) \frac{x^3}{3} \dots \right]. \end{aligned} \quad (8.13)$$

Finally, we can express r to second order in z by dividing (8.13) successively through by (8.12). We find

$$r = \left(\frac{c}{H_0}\right) \left[z - \frac{z^2}{2}(1+q_0) + \dots \right]. \quad (8.14)$$

The last step is to evaluate $D = \Re \sin(r/\Re)$ but, since the expansion for small values of r/\Re is

$$D = r \left(1 - \frac{1}{6} \frac{r^2}{\Re^2}\right), \quad (8.15)$$

the dependence upon the curvature only appears in third order in z and so to second order, we find the kinematic result

$$D = \left(\frac{c}{H_0}\right) \left[z - \frac{z^2}{2}(1+q_0) \right]. \quad (8.16)$$

Let us now evaluate the comoving radial distance coordinate r and the distance measure D to third order in redshift starting from the full solution of the dynamical field equations, that is, starting from the general result (7.74) for r

$$r = \frac{c}{H_0} \int_0^z \frac{dz}{[(1+z)^2(\Omega_0z+1) - \Omega_\Lambda z(z+2)]^{1/2}}.$$

The denominator of the integral can be reorganised to show explicitly the dependence upon the deceleration parameter q_0 and the present matter density parameter Ω_0 using (8.7)

$$\begin{aligned} r &= \frac{c}{H_0} \int_0^z \frac{dz}{[1 + (2 + \Omega_0 - 2\Omega_\Lambda)z + (1 + 2\Omega_0 - \Omega_\Lambda)z^2 + \Omega_0z^3]^{1/2}} \\ &= \frac{c}{H_0} \int_0^z \frac{dz}{[1 + 2(1 + q_0)z + (1 + \frac{3}{2}\Omega_0 + q_0)z^2 + \Omega_0z^3]^{1/2}}. \end{aligned} \quad (8.17)$$

Now expand the denominator to second order for small values of z

$$\begin{aligned} r &= \frac{c}{H_0} \int_0^z \left[1 - z(1+q_0) + \frac{z^2}{2}(2 + 5q_0 + 3q_0^2 - \frac{3}{2}\Omega_0) \right] dz \\ &= \frac{c}{H_0} \left[z - \frac{z^2}{2}(1+q_0) + \frac{z^3}{6}(2 + 5q_0 + 3q_0^2 - \frac{3}{2}\Omega_0) \right]. \end{aligned} \quad (8.18)$$

As before, we form $D = \Re \sin(r/\Re)$, where

$$\Re = \frac{c/H_0}{[(\Omega_0 + \Omega_\Lambda) - 1]^{1/2}} = \frac{c/H_0}{(\frac{3}{2}\Omega_0 - q_0 - 1)^{1/2}}. \quad (8.19)$$

Preserving quantities to third order in z , we find

$$D = \frac{c}{H_0} \left[z - \frac{z^2}{2}(1+q_0) + \frac{z^3}{6}(3 + 6q_0 + 3q_0^2 - 3\Omega_0) \right]. \quad (8.20)$$

This is the result we have been seeking.

To second order in the redshift, we obtain exactly the same result as that obtained from the kinematic argument (8.16). What this means is that, to second order in redshift, the distance measure D does not depend upon the density parameter Ω_0 at small redshifts, $z \ll 1$; it only depends upon the deceleration, or acceleration, whatever its cause. The physical meaning of this result is that at the greater the deceleration, the closer the source of the radiation is to us and so the smaller the look-back time and the comoving radial distance coordinate of the source. Conversely, if the Universe accelerated between the redshift z and the present epoch, the look-back time τ would be greater and so would the comoving radial distance coordinate r . The negative sign in front of the terms in z^2 in (8.20) formalises these qualitative arguments. It can also be seen from (8.20) that, even to third order in the redshift, the dependence upon the density parameter is quite weak.

One approach to the determination of the kinematics of the Universe is therefore to estimate the deceleration of the Universe by determining the distance measures D for objects at small redshifts, say $z \leq 0.3$, at which there are small but appreciable differences between the world models. This is a very demanding programme, but it may well become feasible with the huge surveys of nearby galaxies undertaken by the AAT 2dF and SDSS teams.

As discussed above, the standard procedure is to determine the $D - z$ relation very precisely to large redshifts and then estimate the parameters Ω_0 and Ω_Λ from the detailed shape of that relation. As an example, the variations of the comoving radial distance coordinate r and the distance measure D are shown as a function of redshift in Fig. 7.6 for a range of flat world models. It can be seen that these relations are of quite different shapes.

The importance of these analyses is that they provide tests of General Relativity

and the laws of physics on the largest scales accessible to us at the present epoch. To

express this thought less cryptically, is the present deceleration or acceleration of the

Universe entirely due to the amount of gravitating matter and dark energy present in

the Universe today?

8.3 Hubble's Constant H_0

Hubble's constant H_0 appears ubiquitously in cosmological formulae and its value was the subject of considerable controversy for many years. The use of the redshift-magnitude relation for brightest cluster galaxies had the advantage that Hubble's law is defined well beyond distances at which there might have been deviations associated with the peculiar motions of clusters and superclusters of galaxies (Fig. 2.11). Therefore, Hubble's constant could be found if the distances to the nearest rich clusters of galaxies could be estimated accurately.

The traditional approach to this calibration involved a hierarchy of distance indicators to extend the local distance scale from the vicinity of the Solar System to the nearest giant cluster of galaxies, the Virgo cluster. The only direct methods of distance measurement involve stellar parallaxes and can only be used for stars in the neighbourhood of the Sun. To extend the distance scale further, it is assumed that objects of the same intrinsic types can be identified at greater distances. Then, their relative brightnesses provide estimates of their distances. Examples of the different techniques used are summarised in Fig. 8.1. The period-luminosity relation for Cepheid variables provides one of the best means of extending the distance scale from our own Galaxy to nearby galaxies. Other techniques were used to extend the distance scale from the neighbourhood of our Galaxy to the Virgo cluster, including the luminosity functions of globular clusters, the brightest stars in galaxies and the luminosities of Type Ia supernovae at maximum light. In 1977, Tully and Fisher discovered the relation between the absolute magnitudes of spiral galaxies and the velocity widths of their 21-cm line emission (Tully and Fisher, 1977). This relation could be determined for a number of spiral galaxies in a nearby group or cluster and then relative distances found by assuming that the same correlation between their intrinsic properties is found in more distant groups and clusters (see Sect. 3.6.3).

From the 1970s until the 1990s, there was an ongoing controversy concerning the value of Hubble's constant. A detailed discussion of the different approaches to the determination of Hubble's constant during the 1970s and 1980s was provided by Rowan-Robinson, his conclusions being updated in 1988 (Rowan-Robinson, 1985, 1988). In a long series of papers, Sandage and Tammann found values of Hubble's constant of about $50 \text{ km s}^{-1} \text{ Mpc}^{-1}$, whereas de Vaucouleurs, Aaronson, Mould and their collaborators consistently found values of about $80 \text{ km s}^{-1} \text{ Mpc}^{-1}$. The nature of the discrepancy can be appreciated from their estimates of the distance to the Virgo cluster. If its distance is 15 Mpc, the higher estimate of H_0 is found, whereas if the distance is 22 Mpc, values close to $50 \text{ km s}^{-1} \text{ Mpc}^{-1}$ are obtained. Sandage and Tammann repeatedly emphasised how sensitive the distance estimates are to observational selection effects, such as the Malmquist effect, namely that intrinsically more luminous galaxies are selected in faint samples of galaxies than in brighter samples, and systematic errors.

During the 1990s, a major effort was made to resolve these differences, much of it stimulated by the capability of the Hubble Space Telescope (HST) to measure Cepheid variable stars in the Virgo cluster of galaxies. When the HST project was approved in 1977, one of its major scientific objectives was to use its superb

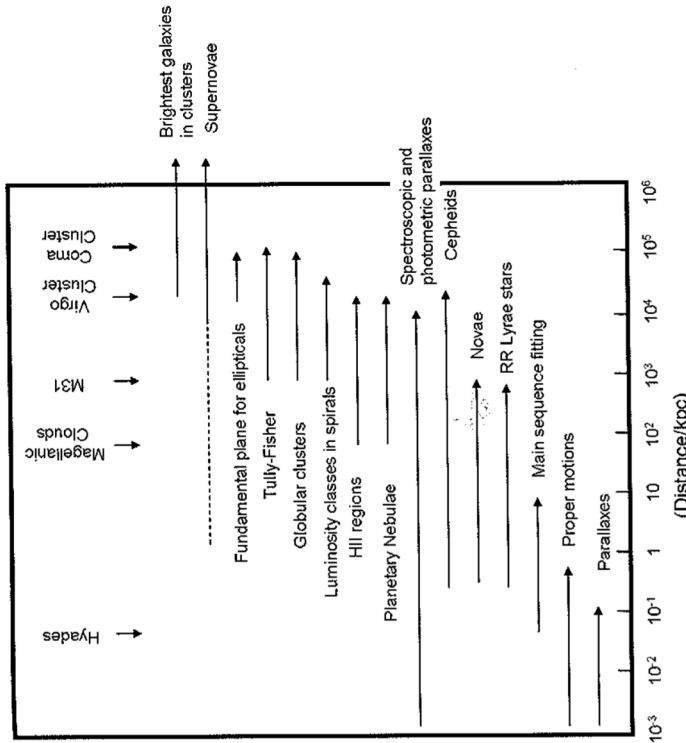


Fig. 8.1. Illustrating the ‘cosmological distance ladder’ (Rowan-Robinson, 1985, 1988). The diagram shows roughly the range of distances over which different classes of object can be used to estimate astronomical distances. The diagram has been redrawn and updated from Rowan-Robinson’s presentation

sensitivity for faint star-like objects to enable the light curves of Cepheid variables in the Virgo cluster to be determined precisely and so estimate the value of Hubble's constant to 10% accuracy. This programme was raised to the status of an HST Key Project in the 1990s with a guaranteed share of observing time to enable a reliable result to be obtained.

The Key Project team, led by Freedman, carried out an outstanding programme of observations and analysis of these data. Equally important was the fact that the team used not only HST data, but also all the other distance measurement techniques to ensure internal self-consistency of the distance estimates. For example, the improved determination of the local distance scale in our own Galaxy from the parallax programmes of the *Hipparcos* astrometric satellite improved significantly the reliability of the calibration of the local Cepheid distance scale. The great advance of the 1990s was that the distances of many nearby galaxies became known very

much more precisely than they were previously. As a result, by 2000, there was relatively little disagreement among the experts about the distances of those galaxies which had been studied out to the distance of the Virgo cluster. If there were differences, they arose from how the data were to be analysed once the distances were known, in particular, in the elimination of systematic errors and biases in the observed samples of galaxies. The final result of the HST Key Project published in 2001 was $72 \pm 8 \text{ km s}^{-1} \text{ Mpc}^{-1}$, where the errors are $1 - \sigma$ errors (Freedman et al., 2001).

In addition to this approach, new physical methods of measuring H_0 became available which have the advantage of eliminating many of the steps involved in the traditional cosmological distance ladder. They are based upon measuring a physical dimension l of a distant object, independent of its redshift, and its angular size θ , so that an angular diameter distance D_A can be found from $D_A = l/\theta$ at a known redshift z . A beautiful example of the use of this technique was described by Panagia and his colleagues who combined IUE observations of the time-variability of the emission lines from the supernova SN 1987A in the Large Magellanic Cloud with Hubble Space Telescope observations of the emission-line ring observed about the site of the explosion to measure the physical size of the ring (Panagia et al., 1991). The distance found for the Large Magellanic Cloud was as accurate as that found by the traditional procedures.

Another promising method, suggested originally by Baade in 1926 and modified by Wesselink in 1947, involves measuring the properties of an expanding stellar photosphere (Baade, 1926; Wesselink, 1947). If the velocity of expansion can be measured from the Doppler shifts of the spectral lines and the increase in size estimated from the change in luminosity and temperature of the photosphere, the distance of the star can be found. The *Baade–Wesselink method* was first applied to supernovae by Branch and Patchett and by Kirshner and Kwan in the 1970s (Branch and Patchett, 1973; Kirshner and Kwan, 1974). It was successfully applied to the supernovae SN 1987A in the Large Magellanic Cloud by Eastman and Kirshner, resulting in a distance consistent with other precise distance measurement techniques (Eastman and Kirshner, 1989). Extending the Baade–Wesselink technique to Type II supernovae with distances ranging from 50 kpc to 120 Mpc, Schmidt and his colleagues found a value of H_0 of $60 \pm 10 \text{ km s}^{-1} \text{ Mpc}^{-1}$ (Schmidt et al., 1992).

Another approach which has produced promising results involves the use of the hot gaseous atmospheres in clusters of galaxies, the properties of which can be measured from their X-ray emission and from the Sunyaev–Zeldovich decrement in the Cosmic Microwave Background Radiation due to inverse Compton scattering. As discussed in Sect. 4.5, clusters of galaxies contain vast quantities of hot gas which is detected by its X-ray bremsstrahlung. The X-ray surface brightness depends upon the electron density N_e and the electron temperature T_e through the relation $I_\nu \propto \int N_e^2 T_e^{-1/2} dl$. The electron temperature T_e can be found from the shape of the bremsstrahlung spectrum. Furthermore, the decrement in the background due to the Sunyaev–Zeldovich effect is proportional to the Compton optical depth $y = \int (kT_e/m_e c^2) \sigma_T N_e dl \propto \int N_e T_e dl$. Thus, the physical properties of the hot gas are

overdetermined and the physical dimensions of the X-ray emitting volume can be found. Bonamente and his colleagues studied 38 clusters of galaxies in the redshift interval $0.14 \leq z \leq 0.89$ using X-ray data from the Chandra X-ray Observatory and measurements of the corresponding Sunyaev–Zeldovich decrements from the Owens Valley Radio Observatory and the Berkeley–Illinois–Maryland Association interferometric arrays (Bonamente et al., 2006). An estimate of Hubble's constant of $H_0 = 76.9^{+3.9}_{-3.4} (\text{stat})^{+10.0}_{-8.0} (\text{syst}) \text{ km s}^{-1} \text{ Mpc}^{-1}$ was found assuming $\Omega_0 = 0.3$ and $\Omega_\Lambda = 0.7$.

Another example of a physical method of measuring H_0 is to use gravitational lensing of distant objects by intervening galaxies or clusters. The first gravitationally lensed quasar 0957+561 was discovered by Walsh, Carswell and Weymann in 1979 (Walsh et al., 1979). The gravitational deflection of the light from the quasar by the intervening galaxy splits its image into a number of separate components, in the case of 0957+561 into two almost identical quasar images (Fig. 8.2). If the background quasar is variable, a time delay is observed between the variability of the different images because of the different path lengths from the quasar to the observer on Earth. For example, a time delay of 418 days has been measured for the two components of the double quasar 0957+561 (Kundic et al., 1997). This observation enables physical scales at the lensing galaxy to be determined, the main uncertainty resulting from the modelling of the mass distribution in the lensing galaxy. In the case of the double quasar 0957+561, Kundic and his colleagues claim

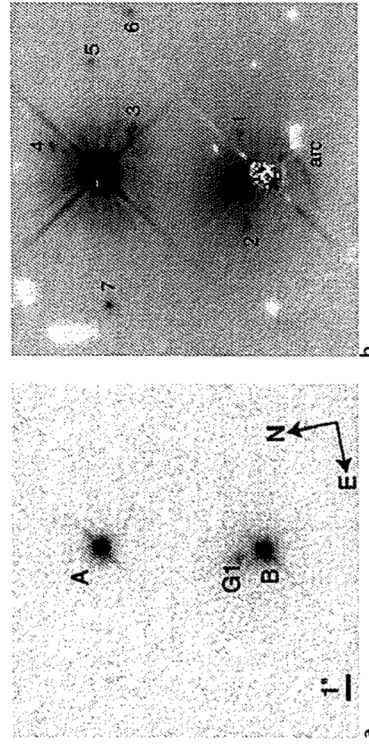


Fig. 8.2a,b. Optical images of the double quasar 0957+561. **a** The system observed in a 80 second exposure made with the WFPC2 camera of the Hubble Space Telescope. The A and B quasar images and the primary lensing galaxy G1 are apparent. **b** A 39,000 second image made with the same camera. A shifted version of the image has been subtracted so that quasar A acts as a template for quasar B. White objects are negative 'ghosts' resulting from the subtraction process. The lensing galaxy is now clearly visible, as are other faint features including the arc to the south of the lensing galaxy (Bernstein et al., 1997)

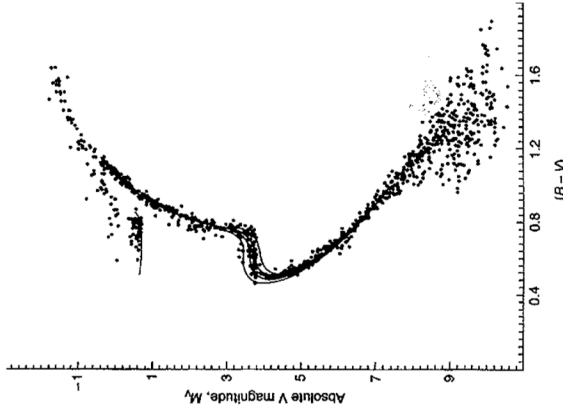


Fig. 8.3. The Hertzsprung–Russell diagram for the globular cluster 47 Tucanae (Hesser et al., 1987). The solid lines show fits to the data using theoretical models of the evolution of stars of different masses from the main sequence to the giant branch due to Vandenberg. The isochrones shown have ages of $10, 12, 14$ and 16×10^9 years, the best-fitting values lying in the range $(12\text{--}14) \times 10^9$ years. The cluster is metal-rich relative to other globular clusters, the metal abundance corresponding to about 20% of the solar value

that the mass distribution in the galaxy is sufficiently well-constrained for the model dependent uncertainties to be small. They derived a value of Hubble's constant of $H_0 = 64 \pm 13 \text{ km s}^{-1} \text{ Mpc}^{-1}$ at the 95% confidence level. A statistical analysis of 16 multiply imaged quasars by Oguri found a value of Hubble's constant of $H_0 = 68 \pm 6 \text{ (stat)} \pm 8 \text{ (syst) km s}^{-1} \text{ Mpc}^{-1}$ (Oguri, 2007).

The estimates of Hubble's constant found by these physical methods, as well as the value determined from studies of the fluctuation spectrum of the Cosmic Microwave Background Radiation (Chap. 15), are consistent with the value of $H_0 = 72 \pm 8 \text{ km s}^{-1} \text{ Mpc}^{-1}$ found by Freedman and her colleagues.

8.4 The Age of the Universe T_0

Globular clusters are among the oldest systems in our Galaxy and so their ages provide lower limits to the age of the Universe. The determination of their ages was pioneered by Sandage and Schwarzschild and involved the comparison of the Hertzsprung–Russell diagrams of the oldest, metal-poor, globular clusters with the expectations of the theory of stellar evolution from the main sequence onto the giant branch (Sandage and Schwarzschild, 1952).

The feature of these diagrams which is particularly sensitive to the age of the cluster is the *main sequence termination point*. In the oldest globular clusters, the main sequence termination point has reached a mass of about $0.9 M_\odot$ and in the most metal-poor, and presumably oldest, clusters the abundances of the elements with $Z \geq 3$ are about 150 times lower than their Solar System values. These facts make the determination of stellar ages much simpler than might be imagined. As Bolte has pointed out, low mass, metal-poor stars have radiative cores and so are unaffected by the convective mixing of unprocessed material from their envelopes into their cores (Bolte, 1997). Furthermore, the corrections to the perfect gas law equation of state are relatively small throughout most solar mass stars. Finally, the surface temperatures of these stars are high enough for molecules to be rare in their atmospheres, simplifying the conversion of their effective temperatures into predicted colours. Taking account of the various sources of uncertainty, Chaboyer demonstrated that the absolute magnitude of the main sequence termination point is the best indicator of the age of the cluster (Chaboyer, 1998).

As understanding of the theory of stellar evolution has advanced, improved estimates of the ages of the oldest globular clusters have become available. A good example of what can be achieved is illustrated in Fig. 8.3 which shows a comparison of the Hertzsprung–Russell diagram for the old globular cluster 47 Tucane with the predicted isochrones for various assumed ages for the cluster. In this case the abundance of the heavy elements is only 20% of the Solar abundance and the age of the cluster is estimated to be between $(12\text{--}14) \times 10^9$ years (Hesser et al., 1987).

In 1994, Maeder reported evidence that the ages of the oldest globular clusters are about 16×10^9 years (Maeder, 1994) and similar results were reported by Sandage

in 1995 (Sandage, 1995). In 1997, Bolte argued that the ages of the oldest globular clusters were

$$T_0 = 15 \pm 2.4 \text{ (stat)} \quad {}^{+4}_{-1} \text{ (syst) Gyr.} \quad (8.21)$$

The first results of the *Hipparcos* astrometric survey relating to the determination of the local distance scale were announced in 1997, with the result that it increased by about 10% (Feast and Catchpole, 1997). This result meant that the stars in globular clusters were more luminous than previously thought and so their main sequence lifetimes were reduced. In Chaboyer's review of 1998, the ages of globular clusters were estimated to be $T_0 = (11.5 \pm 1.3)$ Gyr (Chaboyer, 1998).

Constraints on the age of the Galaxy can also be obtained from estimates of the cooling times for white dwarfs. According to Chaboyer, these provide a firm lower limit of 8 Gyr. The numbers of white dwarfs observed in the vicinity of the Solar System enable an estimate of $(9.5^{+1.1}_{-0.8})$ Gyr to be made for the age of the disc of our Galaxy (Oswalt et al., 1996).

In 1904, Rutherford used the relative abundances of radioactive species to set a lower limit to the age of the Earth of 700 million years, in the process demolishing the Kelvin–Helmholtz picture of stellar evolution (Rutherford, 1907). Using similar techniques, lower limits to the age of the Universe can be derived from the discipline

of *nucleocosmochronology*. A secure lower limit to the age of the Universe can be derived from the abundances of long-lived radioactive species. In 1963 Anders used these to determine an accurate age for the Earth of 4.6×10^9 years (Anders, 1963). Some pairs of long-lived radioactive species, such as ^{232}Th - ^{238}U , ^{235}U - ^{238}U , and ^{187}Re - ^{187}Os can provide information about nucleosynthetic time-scales before the formation of the Solar System (Schramm and Wasserburg, 1970). These pairs of elements are all produced by the r-process in which the time-scale for neutron capture is less than the β -decay lifetime. The production abundances of these elements can be predicted and compared with their present observed ratios (Cowan et al., 1991).

The best astronomical application of this technique has been carried out by Sneden, Cowan and their colleagues for the ultranatal-poor K giant star CS 22892-052 in which the iron abundance is 1000 times less than the solar value (Sneden et al., 1992). A number of species never previously observed in such metal-poor stars were detected, for example, Th (terbium, $Z = 67$), Ho (holmium, $Z = 67$), Tm (thulium, $Z = 69$), Hf (hafnium, $Z = 72$) and Os (osmium, $Z = 76$), as well a single line of Th (thorium, $Z = 90$). The thorium abundance is significant smaller than its scaled solar system abundance and so the star must have been formed much earlier than the Solar System. A lower limit to the age of CS 22892-052 of $(15.2 \pm 3.7) \times 10^9$ years was found.

A conservative lower bound to the cosmological time-scale can be found by assuming that all the elements were formed promptly at the beginning of the Universe. From this line of reasoning, Schramm found a lower limit to the age of the Galaxy of 9.6×10^9 years (Schramm, 1997). The best estimates of the age of the Galaxy are somewhat model-dependent, but typically ages of about $(12\text{--}14}) \times 10^9$ years are found (Cowan et al., 1991).

8.5 The Deceleration Parameter q_0

The hope of the pioneers of observational cosmology was that the value of q_0 could be found from studies of distant galaxies through the redshift-apparent magnitude relation, the angular diameter-redshift relation or the number counts of galaxies. This programme proved to be very much more difficult than the pioneers had expected. By the beginning of the twenty-first century, however, real progress was made by two rather different routes, one involving the use of supernovae of Type Ia and the other observations of the spectrum of fluctuations in the Cosmic Microwave Background Radiation.

The major problem encountered by many of the traditional approaches concerned the evolution with cosmic time of the properties of the objects studied and it is salutary to review exactly what went wrong.

8.5.1 The Redshift-Magnitude Relation for the Brightest Galaxies in Clusters

The redshift-apparent magnitude relation for the brightest galaxies in clusters shows an impressive linear relation (Fig. 2.11), but it only extends to redshifts $z \sim 0.5$ at which the differences between the world models are still relatively small (Sandage,

1968). Sandage was well aware of the many effects which needed to be considered before a convincing estimate of q_0 could be found. Some of these were straightforward, such as the need to determine the luminosities of galaxies within a given metric diameter, but others were more complex. For example, as discussed in Sect. 4.2.3, Sandage and Hardy discovered that the brightest galaxy in a cluster is more luminous, the greater the difference in magnitude between the brightest and next brightest galaxies in the cluster (Sandage and Hardy, 1973). In what they termed the *Bautz-Morgan effect*, the second and third ranked members of the cluster were intrinsically fainter than the corresponding galaxies in other clusters with less dominant first ranked galaxies. It seemed as though the brightest galaxy became brighter at the expense of the next brightest members, a phenomenon which could plausibly be attributed to the effects of galactic cannibalism (Hausman and Ostriker, 1977). Sandage adopted an empirical correction to reduce the clusters to a standard Bautz-Morgan type.

Sandage was also well aware of the need to take account of the evolution of the stellar populations of the galaxies with cosmic time. These corrections followed naturally from his work on the Hertzsprung-Russell diagrams of globular clusters of different ages which mimic the cosmic evolution of the old stellar populations of galaxies. He included evolutionary corrections in the K-corrections to the absolute magnitudes of the galaxies. There were, however, other worrying pieces of evidence which did not fit easily into a picture of the passive evolution of galaxies in clusters. Dramatic evidence for the evolution of galaxies in rich, regular clusters at relatively small redshifts was first described in the pioneering analyses of Butcher and Oemler. They found that the fraction of blue galaxies in such clusters increased from less than 5% in a nearby sample to percentages as large as 50% at redshift $z \sim 0.4$ (Butcher and Oemler, 1978, 1984). The Butcher-Oemler effect has been the subject of a great deal of study and debate, the major observational problems concerning the contamination of the cluster populations by foreground and background galaxies, as well as bias in the selection criteria for the clusters selected for observation (Dressler, 1984).

The determination of q_0 might seem to be easier if the samples of galaxies extended to larger redshifts, but it proved far from trivial to find suitable clusters at redshifts greater than 0.5. Those in which the brightest galaxies were observed often turned out to be bluer than expected. This finding reflects a basic problem with this approach to measuring the deceleration parameter: the differences between the expectations of the world models only become appreciable at large redshifts at which the Universe was significantly younger than it is now. Consequently careful account has to be taken of the evolutionary changes of the objects which are assumed to have ‘standard’ properties.

By the time of Sandage’s review of the problem in 1993, the uncertainties in the value of q_0 had not decreased, his estimate being $q_0 = 1 \pm 1$ (Sandage, 1995). In fact, by that time, Argón-Salamanca, Ellis and their colleagues had extended the infrared redshift-apparent magnitude relation for the brightest galaxies in clusters to redshift $z = 0.9$ (Argón-Salamanca et al., 1993). They found evidence that the galaxies were bluer at the larger redshifts, but, perhaps surprisingly, that their redshift-apparent magnitude relation followed closely a model with $q_0 = 1$ with no

corrections for the evolution of the stellar populations of the galaxies, for cluster richness or for Bautz-Morgan type.

8.5.2 The Redshift–Magnitude Relation for Radio Galaxies

Another approach to extending the redshift–apparent magnitude relation to large redshifts became possible in the early 1980s when the use of the first generation of CCD cameras enabled complete samples of bright 3CR radio sources to be identified with very faint galaxies. These galaxies turned out to have very strong, narrow emission line spectra and spectroscopy by Hyron Spinrad and his colleagues showed that many of these radio galaxies had very large redshifts. These observations showed that the 3CR radio galaxies are among the most luminous galaxies known.

At about the same time, infrared photometry of these galaxies in the 1–2.2 μm waveband became feasible with the development of sensitive indium antimonide detectors. There were several advantages in defining the redshift–apparent magnitude relation in the K waveband at 2.2 μm , one of them being that dust becomes transparent in the near-infrared waveband and so extinction corrections to the luminosities of the galaxies are very small. A second advantage is that the stars which contribute most of the luminosity at these wavelengths belong to the old red giant population of the galaxy. As a result, the magnitudes are not affected by bursts of star formation which can profoundly influence the optical magnitudes of the galaxies and which is largely responsible for the fact that the galaxies at redshifts greater than 0.5 are significantly bluer than those observed at lower redshifts (see Sect. 17.2.2).

In 1984, Lilly and I determined the redshift–apparent magnitude relation for a complete sample of 3CR radio galaxies at an infrared wavelength of 2.2 μm (Fig. 8.4) (Lilly and Longair, 1984). We found that there is a remarkably well-defined K magnitude–redshift relation which extended to redshifts of 1.5. It was also clear that the galaxies at large redshifts were more luminous than expected for world models with $q_0 \sim 0$ –0.5. When simple evolutionary corrections were made for the increased rate at which stars evolved onto the giant branch at earlier epochs (Sect. 17.2.2), values of q_0 in the range 0 to 1 were found. This appeared to be evidence for the evolution of the stellar populations of these galaxies over cosmological time-scales.

There were, however, problems with this simple picture. In the late 1980s, Chambers, Miley, McCarthy and their collaborators discovered the alignment of the radio structures with the optical images of the 3CR galaxies and this complicated the interpretation of these data (Chambers et al., 1987; McCarthy et al., 1987). Optical images taken with the Hubble Space Telescope and ground-based infrared images taken with the UK Infrared Telescope of five of the 3CR radio galaxies in the redshift interval $1 < z < 1.3$ are shown in Fig. 8.5 (Best et al., 1996). The infrared images in the right-hand column look exactly like the classic picture of a double radio source associated with a giant elliptical galaxy. In the HST images in the left-hand column, however, a wide variety of high surface brightness structures is observed aligned with the radio structures – the optical images of the radio galaxies are quite unlike the symmetric structure of giant elliptical galaxies. Our optical spectroscopic observations of the aligned structures seen in the five radio galaxies in Fig. 8.5

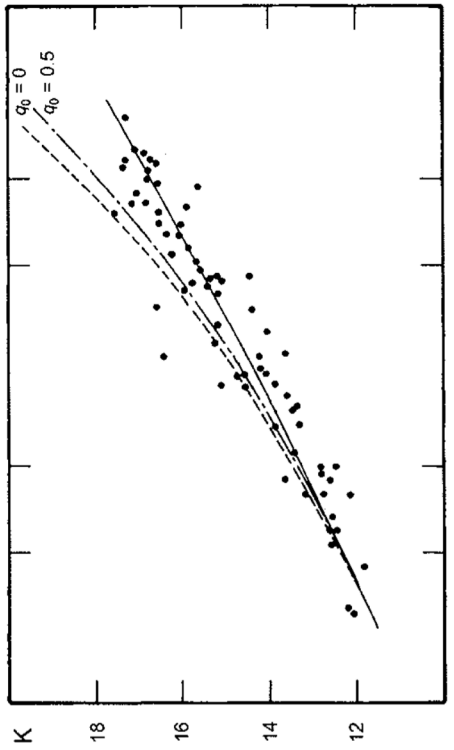


Fig. 8.4. The K magnitude–redshift relation for a complete sample of narrow line radio galaxies from the 3CR catalogue. The infrared apparent magnitudes were measured at a wavelength of 2.2 μm . The dashed lines show the expectations of world models with $q_0 = 0$ and $\frac{1}{2}$. The solid line is a best-fitting line for standard world models with $\Omega_\Lambda = 0$ and includes the effects of stellar evolution of the old stellar population of the galaxies (Lilly and Longair, 1984)

showed that they are shock-excited gas clouds, probably associated with the strong shocks created by the passage of the radio jets through the intergalactic medium surrounding the radio galaxy (Best et al., 2000).

Using a combination of surface photometry of these galaxies in the optical and infrared wavebands, we were able to show that the alignment effect does not have a strong influence upon the K magnitude–redshift relationships (Best et al., 1998). More serious was the fact that surveys of fainter samples of 6C radio galaxies by Eales, Rawlings and their colleagues found that, although the K magnitude–redshift relation agreed with our relation at redshifts less than 0.6, their sample of radio galaxies at redshifts $z \sim 1$ were significantly less luminous than the 3CR galaxies by about 0.6 magnitudes (Eales et al., 1997). Our most recent analysis of these data for a preferred cosmological model with $q_0 = 0.3$ and $\Omega_\Lambda = 0.7$, including corrections for the evolution of their stellar populations, have demonstrated that 3CR radio galaxies at redshifts $z \geq 0.6$ are indeed significantly more luminous than their nearby counterparts (Inskip et al., 2002). Our apparent success in accounting for the K magnitude–redshift relation for 3CR radio galaxies in the 1980s was an unfortunate cosmic conspiracy.

The lesson of this story is that the selection of galaxies as standard objects at large redshifts is a hazardous business; we generally learn more about the astrophysics and astrophysical evolution of the galaxies rather than about cosmological parameters.

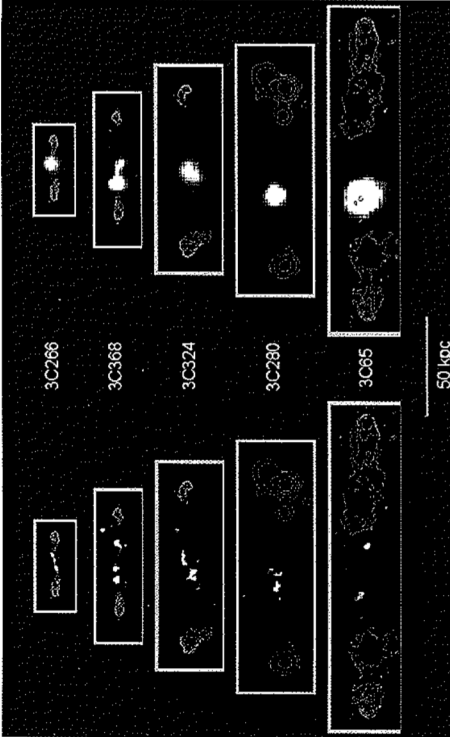


Fig. 8.5. HST (left) and UKIRT (right) images of the radio galaxies 3C 266, 368, 324, 280 and 65 with the VLA radio contours superimposed (Best et al., 1996). The images are drawn on the same physical scale. The angular resolution of the HST images is 0.1 arcsec while that of the ground-based infrared images is about 1 arcsec

8.5.3 The Redshift–Magnitude Relation for Type Ia Supernovae

The discussion of Sect. 7.4.5 makes it clear that what is required is a set of standard objects which are not susceptible to poorly understood evolutionary changes with cosmic epoch. The use of supernovae of Type Ia to extend the redshift–apparent magnitude relation to redshifts $z > 0.5$ has a number of attractive features. First of all, it is found empirically that these supernovae have a very small dispersion in absolute luminosity at maximum light (Branch and Tammann, 1992). This dispersion can be further reduced if account is taken of the correlation between the maximum luminosity of Type Ia supernovae and the duration of the initial outburst. This correlation, referred to as the *luminosity–width relation*, is in the sense that the supernovae with the slower decline rates from maximum light are more luminous than those which decline more rapidly (Phillips, 1993). Secondly, there are good astrophysical reasons to suppose that these objects are likely to be good standard candles, despite the fact that they are observed at earlier cosmological epochs. The preferred picture is that these supernovae result from the explosion of white dwarfs which are members of binary systems which accrete mass from the other member of the binary. Although the precise mechanism which initiates the explosion has not been established, the favoured picture is that mass accreted onto the surface of the white dwarf raises the temperature of the surface layers to such a high temperature that nuclear burning is initiated and a deflagration front propagates into the interior of

the star, causing the explosion which results in its destruction. It is entirely plausible that these types of explosion should have uniform properties.

In 1995 Ariel Goobar and Saul Perlmutter discussed the feasibility of observing Type Ia supernova out to redshift $z \approx 1$ in order to estimate the values of Ω_0 and Ω_A (Goobar and Perlmutter, 1995). In 1996, they and their colleagues described the first results of systematic searches for Type Ia supernovae at redshifts $z \sim 0.5$ using an ingenious approach to detect them before they reached maximum light (Perlmutter et al., 1996). Deep images of selected fields, including a number which contain distant clusters of galaxies, were taken during one period of new moon and the fields were then imaged in precisely the same way during the next new moon. Using rapid image analysis techniques, any supernovae which appeared between the first and second epoch observations were quickly identified and reobserved photometrically and spectroscopically over the succeeding weeks to determine their types and light curves.

Using this search technique, Perlmutter and his colleagues discovered 27 supernovae of Type Ia between redshifts 0.4 and 0.6 in three campaigns in 1995 and 1996 (Perlmutter et al., 1996, 1997). The team used these and subsequent data to demonstrate convincingly the effects of cosmological time dilation by comparing the light curves of Type Ia supernovae at redshifts $z \sim 0.4$ –0.8 with those of the same type at the present epoch, thus testing directly the cosmological time dilation–redshift relation (Goldhaber et al., 2001) (see Fig. 5.7). The same peak luminosity–width correlation was found as that observed at small redshifts. When account was taken of this relation, the intrinsic spread in the luminosities of the Type Ia supernovae was only 0.21 magnitudes.

This same technique has been used to discover Type Ia supernovae at redshifts greater than $z = 0.8$ as a result of observations with the Hubble Space Telescope. In two independent programmes, Garnavich, Perlmutter and their colleagues discovered the Type Ia supernovae SN1997ck at redshift $z = 0.97$ and SN1997ap at redshift $z = 0.83$ respectively (Garnavich et al., 1998; Perlmutter et al., 1998). The great advantage of the HST observations is that their high angular resolution enables very accurate photometry to be carried out on stellar objects in distant galaxies.

The redshift–apparent magnitude relation presented by Wood-Vasey and his colleagues was derived from the combined ESSENCE and Supernova Legacy Survey data (Fig. 8.6). This compilation has resulted in a redshift–apparent magnitude relation similar to that found by Perlmutter, Garnavich and their colleagues, but with much larger statistics (Wood-Vasey et al., 2007). The solid line shows a best-fitting theoretical curve (solid line) which has cosmological parameters $\Omega_0 = 0.27$ and $\Omega_A = 0.73$. The major result of these observations, which has been found by the independent groups, is that the data favour cosmological models in which Ω_A is non-zero. This was the first time in the history of observational cosmology that compelling evidence for a finite value of the cosmological constant has been found. The groups have continued to extend this technique to large redshifts through the discovery of Type Ia supernovae at very large redshifts (Knop et al., 2003; Tonry et al., 2003). The best presentation of these results is in terms of a diagram in which

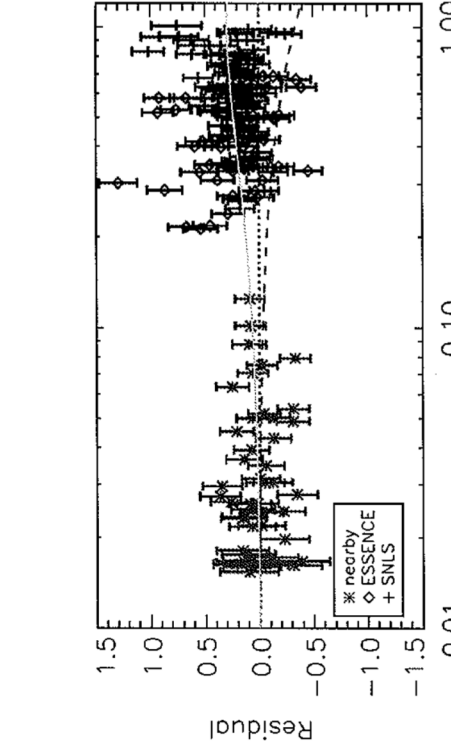
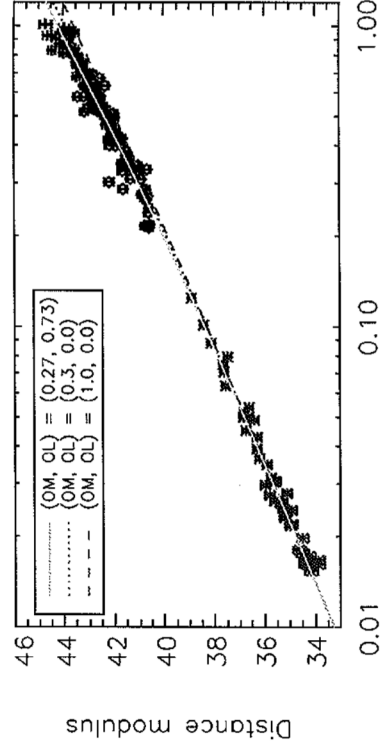


Fig. 8.6. The luminosity distance-redshift relation for supernovae of Type Ia from the combined ESSENCE and Supernova Legacy Survey data. For comparison the overplotted *solid line* and *residuals* are for a Λ CDM model with $w = -1$, $\Omega_0 = 0.27$ and $\Omega_\Lambda = 0.73$. The *dotted* and *dashed lines* are for models with $\Omega_\Lambda = 0$, as indicated in the figure legend (Wood-Vasey et al., 2007)

the density parameter of the matter content of the Universe Ω_0 is plotted against Ω_Λ . The results of the Supernova Cosmology Project are shown in Fig. 8.7. There are various ways of interpreting Fig. 8.7, particularly when taken in conjunction with independent evidence on the mean mass density of the Universe and the evidence from the spectrum of fluctuations in the Cosmic Microwave Background

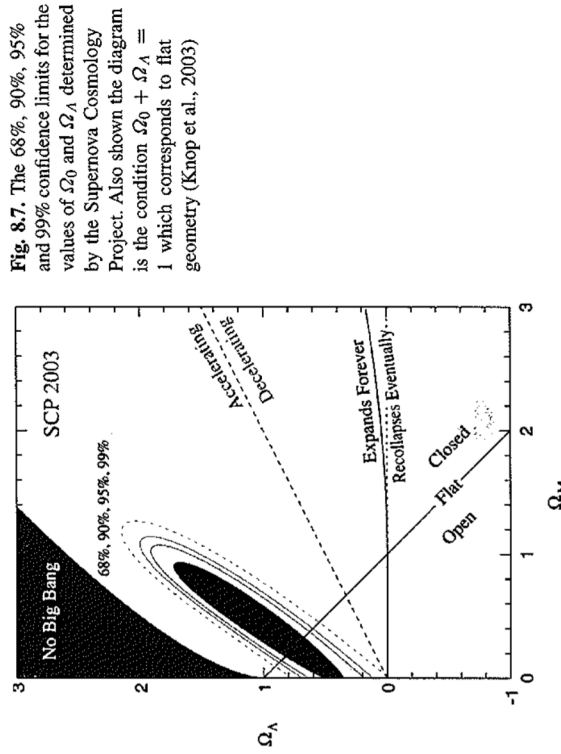


Fig. 8.7. The 68%, 90%, 99% and 99% confidence limits for the values of Ω_0 and Ω_Λ determined by the Supernova Cosmology Project. Also shown the diagram is the condition $\Omega_0 + \Omega_\Lambda = 1$ which corresponds to flat geometry (Knop et al., 2003)

8.5.4 The Number Counts of Galaxies

In his assessment of approaches to the determination of cosmological parameters, Sandage was not optimistic about the use of the number counts of galaxies (Sandage, 1961a):

Galaxy counts are insensitive to the model . . . There seems to be no hope of finding q_0 from the $N(m)$ counts because the predicted differences between the models are too small compared with the known fluctuations of the distribution.

These concerns have been fully justified by subsequent studies. The determination of precise counts of galaxies has proved to be one of the more difficult areas of observational cosmology. Ellis has provided an excellent account of the problems of determining and interpreting the counts of faint galaxies (Ellis, 1997). The reasons for these complications are multifold. First of all, galaxies are extended objects, often with complex brightness distributions, and great care must be taken to ensure that

the same types of object are compared at different magnitude limits and redshifts. Furthermore, the distribution of galaxies is far from uniform on scales less than about $50 h^{-1}$ Mpc, as illustrated by the large voids and walls seen in Figs. 2.7 and 2.8. Even at the faintest magnitudes, this ‘cellular’ structure in the distribution of galaxies results in fluctuations in the number counts of galaxies which exceed the statistical fluctuations expected in a random distribution (see Sect. 17.7). In addition, the probability of finding galaxies of different morphological types depends upon the galaxy environment. Finally, the luminosity function of galaxies is quite broad (Figs. 3.14 to 3.16) and so the differences between models are masked by the convolution of the predictions of the world models with this function.

Up till about 1980, the deepest counts extended to apparent magnitudes of about 22 to 23, and, although there were disagreements between the results of different observers, there was no strong evidence that the counts of galaxies departed from the expectations of uniform world models. Since that time, much deeper number counts have been determined thanks to the use of large area CCD cameras on large telescopes, as well as the spectacular images obtained from the Hubble Deep Field (Sect. 7.7).

Up to 23 and, although there were disagreements between the results of different observers, there was no strong evidence that the counts of galaxies departed from the expectations of uniform world models. Since that time, much deeper number counts have been determined thanks to the use of large area CCD cameras on large telescopes, as well as the spectacular images obtained from the Hubble Deep Field (Sect. 7.7).

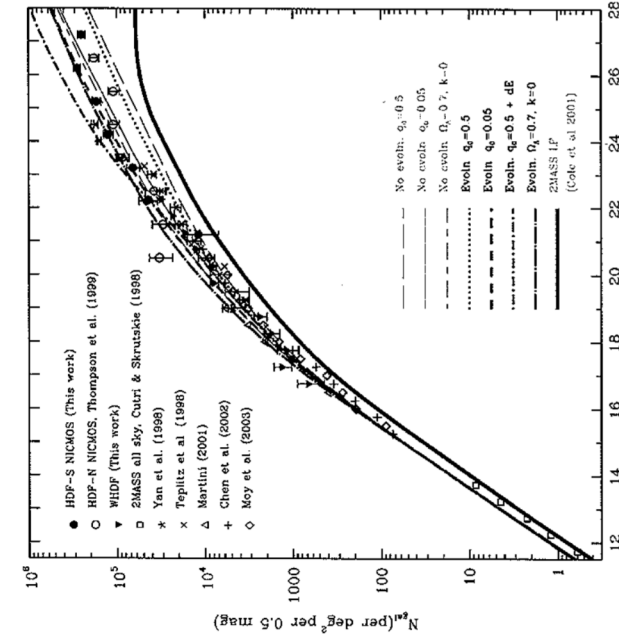


Fig. 8.8. Galaxy number counts in the infrared H waveband ($1.65 \mu\text{m}$) to $H = 28$ magnitude compiled by Metcalfe and his colleagues. The predictions of the various evolving and non-evolving models discussed by them are also shown (Metcalfe et al., 2006)

and the Hubble Ultra-Deep Field. An example of a compilation of deep counts of galaxies in the blue (B), red (I) and infrared (K) wavebands is shown in Fig. 2.12 (Metcalfe et al., 1996). It can be seen that there is a large excess of faint galaxies at blue magnitudes greater than about 22 while the counts of galaxies at red and infrared wavelengths show rather more modest evolution. The counts in the infrared H waveband in particular show little evidence for evolution, but various predictions for models with evolving and non-evolving galaxy populations indicate the real difficulties of determining cosmological parameters by this means (Fig. 8.8). While there is little prospect of using these observations to determine cosmological parameters, they are of the greatest interest in studying the astrophysical evolution of galaxies with cosmic epoch and this topic will be taken up in Chaps. 17 and 19.

8.5.5 The Angular Diameter–Redshift Test

The angular diameter–redshift relation provides an attractive route for the determination of cosmological parameters if accurate proper distances l of astronomical objects can be measured at large redshifts and their corresponding angular sizes θ measured. Then, the angular diameter distance $D_A = l/\theta$ can be determined as a function of redshift and compared with the predictions of the standard world models. The physical methods of measuring proper distances at large redshifts described in Sect. 8.3, involving the Sunyaev–Zeldovich effect in conjunction with X-ray observations of the hot gas in clusters, gravitational lenses and the various versions of the Baade–Wesselink method, all provide means of undertaking this test. A possible problem with this programme is the extent to which the predicted angular diameter–redshift relations are modified by inhomogeneities in the distribution of mass along the line of sight, which can significantly change the predicted relations (Sect. 7.7).

The alternative approach is to use objects which may be considered to be ‘rigid rods’, but the problem is to find suitable metric sizes which can be used in the test. A distinctive feature of this test is the predicted minimum angular diameter as the objects are observed at large redshifts (Fig. 7.8). A good example is the use of the separation of the radio components of double radio sources, such as those illustrated in Fig. 8.5. Large samples of these objects can be found spanning a wide range of redshifts. This test was first carried out by Miley who used the largest angular size of the radio structures of radio galaxies and quasars as a ‘rigid rod’ (Miley, 1968, 1971), but no minimum was found in the observed relation. Kapahi confirmed this result using instead the median angular separation θ_m of the radio source components as a function of redshift (Kapahi, 1987), but again no minimum was found (Fig. 8.9a). The median angular separation of the source components is observed to be roughly inversely proportional to redshift and this was interpreted as evidence that the median physical separation of the source components l_m was smaller at large redshifts. Examples of fits to the observational data using evolution functions of the form $l_m \propto (1+z)^{-n}$ are shown in Fig. 8.9a for world models with $q_0 = 0$ and 0.5; values of $n \approx 1.5$ –2.0 can provide good fits to the data. There are many reasons why the separation of the radio source components might be smaller

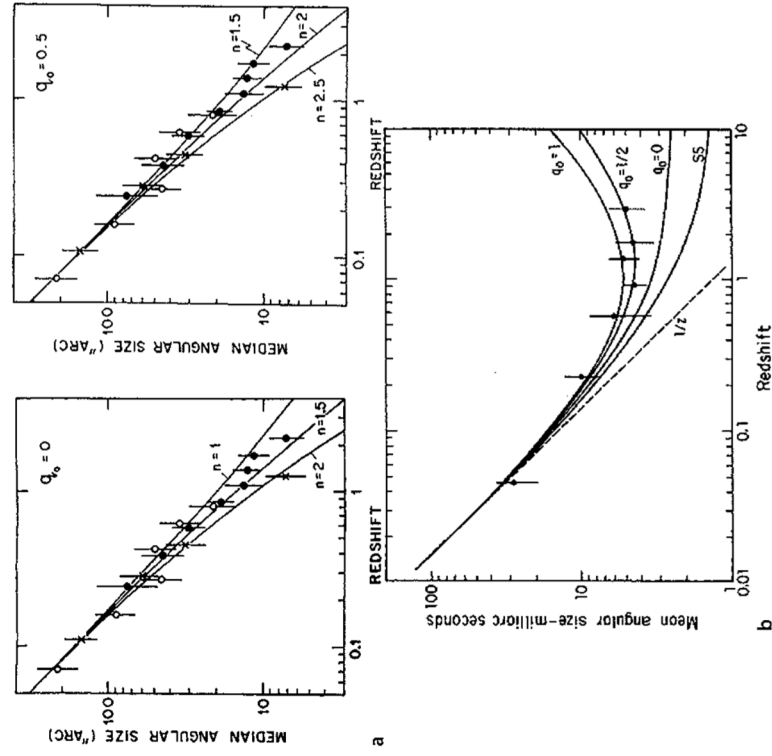


Fig. 8.9. **a** The angular diameter–redshift relation for double radio sources, in which the median angular separation of the double radio source components θ_m is plotted against redshift (Kapahi, 1987). The observed relation follows closely the relation $\theta_m \propto z^{-1}$. The left-hand panel shows fits to the observations for a world model with $q_0 = 0$ and the right-hand panel for a model with $q_0 = 0.5$, in both cases, the median separation of the components being assumed to change with redshift as $l_m \propto (1+z)^{-n}$. **b** The mean angular diameter–redshift relation for 82 compact radio sources observed by VLBI (Kellermann, 1993). In addition to the standard Friedman models, the relation for steady state cosmology (SS) as well as the relation $\theta \propto z^{-1}$ (dashed line) are shown

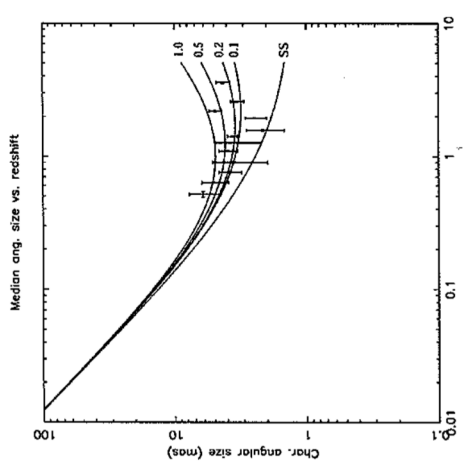


Fig. 8.10. The median angular diameter–redshift relation for 145 high luminosity compact radio sources observed by VLBI (Gurvits et al., 1999). The notation is the same as Fig. 8.9b

Another version of the same test was described by Kellermann and involved using only compact double radio structures studied by Very Long Baseline Interferometry (Kellermann, 1993). He argued that these sources are likely to be less influenced by changes in the properties of the intergalactic and interstellar gas, since the components are deeply embedded within the central regions of the host galaxy. In his angular diameter–redshift relation, there is evidence for a minimum in the relation, which would be consistent with a value of $q_0 \sim 0.5$ (Fig. 8.9b). A problem with this analysis is that the sources at small redshifts are less luminous than those at large redshift. Gurvits and his colleagues repeated the analysis with a much larger sample of 330 compact radio quasars from which they selected a subsample of 145 high luminosity quasars with $L \geq 10^{26} \text{ W Hz}^{-1}$ (Gurvits et al., 1999). The resulting angular diameter–redshift relation shown in Fig. 8.10 shows the large scatter when the data were binned into 12 bins, each with 12–13 sources. As they comment:

None of the solid lines represents the best fit.

Presumably, the properties of the sources are determined by local physical conditions close to the quasar nucleus. In addition, there is a clear lack of high luminosity sources at small redshifts which would ‘anchor’ the relation.

8.6 Ω_A and the Statistics of Gravitational Lenses

One way of testing models with finite values of Ω_A is to make use of the fact that the volume enclosed by redshift z increases as Ω_A increases, as illustrated by Fig. 7.1b for the case $\Omega_0 + \Omega_A = 1$. The statistics of gravitationally lensed images by intervening galaxies therefore provides an important test of models with finite Ω_A .

in the past, for example, the ambient interstellar and intergalactic gas may well have been greater in the past and so the source components could not penetrate so far through the surrounding gas. Again, we learn more about astrophysical changes with cosmic epoch of the objects studied rather than about cosmological parameters.

The power of this approach is illustrated by the following calculation (Fukugita et al., 1992). We assume, for simplicity, that we can represent the population of lensing galaxies by identical isothermal spheres which have constant comoving space density N_0 . We can then use the calculation which resulted in (4.63) for the Einstein radius θ_E , within which strong distortions of the image of a background object are expected,

$$\theta_E = \frac{4\pi \langle v_{||}^2 \rangle}{c^2} \frac{D_{LS}}{D_s},$$

where $\langle v_{||}^2 \rangle$ is the mean square velocity dispersion along the line of sight of the particles which make up each isothermal sphere, D_s is the angular diameter distance of the background quasar and D_{LS} the angular diameter distance from the lens to the background source. We can therefore write the cross-section σ_E of the isothermal sphere for strong lensing as

$$\sigma_E = \pi D_L^2 \theta_E^2 = A \left(\frac{D_L D_{LS}}{D_s} \right)^2, \quad (8.22)$$

where D_L is the angular diameter distance of the isothermal sphere, or lens. We now work out the probability that a background quasar at redshift z_s is observed to be strongly lensed. From (5.73), the number of isothermal spheres in the redshift interval z to $z + dz$ per steradian is

$$dN = N_0 D^2 dr, \quad (8.23)$$

where D is the distance measure which is related to the angular diameter distance by $D_A = D/(1+z)$. Therefore, the probability of strong lensing in the redshift interval dz is given by the total solid angle subtended by all the isothermal spheres in the increment of comoving radial distance coordinate dr

$$p(z) dz = \frac{N_0 \sigma_E D^2}{D_A^2} dr = \frac{N_0 \sigma_E D^2}{[D/(1+z)]^2} dr = N_0 \sigma_E (1+z)^2 dr. \quad (8.24)$$

We integrate this result from $z = 0$ to z_s to obtain the desired probability:

$$p(z_s) = A N_0 \int_0^{z_s} \left(\frac{D_L D_{LS}}{D_s} \right)^2 (1+z)^2 dr. \quad (8.25)$$

In general, dr is given by the expression

$$dr = \frac{c dz}{H_0 [(1+z)^2 (\Omega_0 z + 1) - \Omega_A z (z+2)]^{1/2}}, \quad (8.26)$$

and so

$$p(z_s) = A N_0 \int_0^{z_s} \left(\frac{D_L D_{LS}}{D_s} \right)^2 \frac{c (1+z)^2 dz}{H_0 [(1+z)^2 (\Omega_0 z + 1) - \Omega_A z (z+2)]^{1/2}}. \quad (8.27)$$

To integrate this expression we need to evaluate D_{LS} , the angular diameter distance from the lens to the source. Following the reasoning of Sect. 7.5, the appropriate comoving distance coordinate between the epochs corresponding to z_L and z_S is

$$r(z_L, z_S) = - \int_{z_L}^{z_S} \frac{c dt}{a(t)},$$

and then we form the distance measure $D(z_L, z_S)$ and the angular diameter distance $D_A(z_L, z_S)$,

$$D_A(z_L, z_S) = D(z_L, z_S) \frac{1+z_L}{1+z_S} = \frac{\Re}{(1+z_S)} \sin \int_{z_L}^{z_S} \frac{dr}{\Re}. \quad (8.29)$$

Carroll and his colleagues present the results of the integral (8.27) in a pleasant format. They normalise the integral to the probability of lensing in the case of the Einstein-de Sitter model, $\Omega_0 = 1, \Omega_A = 0$ in which case, it is straightforward to show that the probability for any other model becomes

$$p(z_S) = \frac{15 H_0^2}{4 c^2} \left[1 - \frac{1}{(1+z_S)} \right]^{-3} \int_0^{z_S} \left(\frac{D_L D_{LS}}{D_s} \right)^2 \times \frac{(1+z)^2 dz}{[(1+z)^2 (\Omega_0 z + 1) - \Omega_A z (z+2)]^{1/2}}. \quad (8.30)$$

This function is plotted in Fig. 8.11 in the same format as Fig. 7.4, the contours showing the relative lensing probabilities for a quasar at a typical redshift $z_S = 2$. It can be seen that, if $\Omega_A = 0$, as represented by the solid diagonal line, there are only small changes in the probability of lensing. For low values of Ω_0 , the probability increases by about a factor of 2 as compared with the $\Omega_0 = 1$ model. In contrast, the probability of lensing is very strongly dependent upon the value of Ω_A . For example, for the flat world models with $\Omega_0 + \Omega_A = 1$, the probability of lensing increases by almost a factor of ten as Ω_0 changes from 1 to 0.1. This dramatic increase occurs for a number of reasons. First of all, the distance measure D increases with increasing redshift more rapidly in models with low Ω_0 than in models with high Ω_0 and so much greater volumes are encompassed at a given redshift (Fig. 7.11). Second, the combination of parameters $D_L D_{LS}/D_s$ is sensitive to the presence of the cosmological constant which stretches out the angular diameter distance at a given redshift.

To obtain limits to the value of Ω_A from the frequency and properties of gravitational lenses in complete samples of quasars and radio galaxies, modelling of the lens and background source populations needs to be carried out. The probabilities

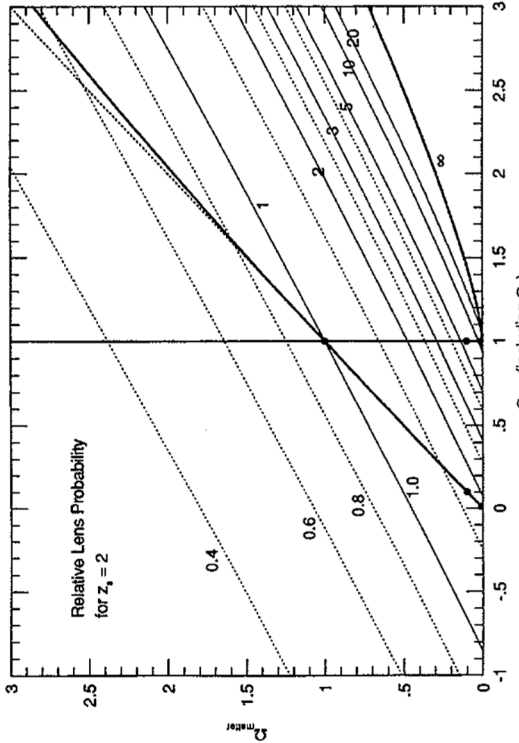


Fig. 8.11. The probability of observing strong gravitational lensing relative to that of the critical Einstein-de Sitter model, $\Omega_0 = 1$, $\Omega_\Lambda = 0$ for a quasar at redshift $z_S = 2$ (Carroll et al., 1992). The contours show the relative probabilities derived from the integral (8.30) and are presented in the same format as in Fig. 7.4

have to be averaged over the luminosity functions of lensing galaxies and the distribution of background sources. Models have to be adopted for the lenses which can account for the observed structures of the lensed images. The amplification of the brightness of the images as well as the detectability of the distorted structures need to be included in the computations. These complications are considered in some detail in the review by Carroll and his colleagues and by Kochanek (Carroll et al., 1992; Kochanek, 1996).

The largest survey to date designed specifically to address this problem has been the Cosmic Lens All Sky Survey (CLASS) in which a very large sample of flat spectrum radio sources was imaged by the Very Large Array (VLA), the Very Long Baseline Array (VLBA) and the MERLIN long baseline interferometer. The sources were selected according to strict selection criteria and resulted in the detection of 13 sources which were multiply imaged out of a total sample of 8958 radio sources (Chae et al., 2002). More recently, the CLASS collaboration has reported the point-source lensing rate to be one per 690 ± 190 targets (Mitchell et al., 2005). The analysis of these data used the luminosity functions for different galaxy types found in the AAT 2dF survey as well as models for the evolution of the population of flat-spectrum radio sources. The CLASS collaboration found that the observed fraction of multiply lensed sources was consistent with flat world models, $\Omega_0 + \Omega_\Lambda = 1$, in

which density parameter in the matter Ω_0 was

$$\Omega_0 = 0.31^{+0.27}_{-0.14} \text{ (68\%)} \quad ^{+0.12}_{-0.10} \text{ (syst).} \quad (8.31)$$

Alternatively, for a flat universe with an equation of state for the dark energy of the form $p = wqc^2$, they found an upper limit to w ,

$$w < -0.55^{+0.18}_{-0.11} \text{ (68\%),} \quad (8.32)$$

consistent with the standard value for the cosmological constant $w = -1$ (Chae et al., 2002).

8.7 The Density Parameter Ω_0

Estimates of the average cosmological density of matter in galaxies were included in Hubble's first paper on the extragalactic nature of the diffuse nebulae. He used his estimates of their average mass-to-light ratios to estimate a mean cosmological density of $\rho_0 = 1.5 \times 10^{-28} \text{ kg m}^{-3}$ (Hubble, 1926). A similar analysis was carried out in 1958 by Oort who found that the average mass density was $3.1 \times 10^{-28} \text{ kg m}^{-3}$ assuming that Hubble's constant was $180 \text{ km s}^{-1} \text{ Mpc}^{-1}$ (Oort, 1958).

In 1978, Gunn expressed the same result in terms of the mass-to-light ratio which would be needed if the Universe were to attain the critical density (Gunn, 1978). He found $(M/L)_{\text{crit}} = 2600h$, very much greater than the values found in our vicinity in the plane of the Galaxy. As described in Sects. 3.5, 4.3 and 4.4, the mass of dark matter in galaxies and clusters of galaxies far exceeds that in the visible parts of galaxies. If account is taken of the dark matter, the overall mass-to-luminosity ratio attains values of $M/L \sim 100-150$. In well-studied rich clusters, such as the Coma cluster, the value of M/L is of the order of 250, but this value is biased towards elliptical and S0 galaxies which have three times larger values of M/L than the spiral galaxies, the latter contributing most of the light per unit volume in the Universe at large. These values of M/L are significantly less than the value needed to close the Universe. Gunn's best estimate of the density parameter for bound systems such as galaxies, groups and clusters of galaxies was about 0.1 and was independent of the value of h .

In 2000, Bahcall reviewed the many different approaches which can be taken to derive values of M/L for clusters of galaxies – cluster mass-to-light ratios, the baryon fraction in clusters and studies of cluster evolution (Bahcall, 2000). These have all found the same consistent result that the mass density of the universe corresponds to $\Omega_0 \approx 0.25$ and furthermore that the mass approximately traces light on large scales. These results reflect the generally accepted view that, if mass densities are determined for bound systems, the total mass density in the Universe is about a factor of 4 less than that needed to close the Universe.

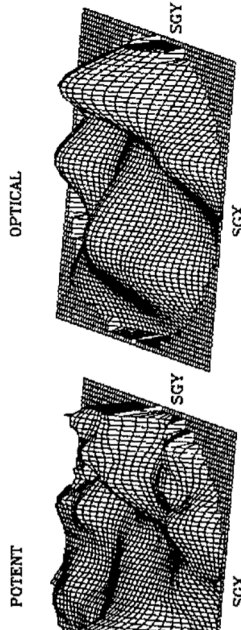


Fig. 8.12. Surface density plots of the density field in the local Supergalactic plane. The left-hand panel shows the mass distribution reconstructed from the peculiar velocity and distance information for the galaxies in this region using the POTENT numerical procedure. The right-hand panel shows the density field of optical galaxies, both images smoothed with a Gaussian filter of radius 1200 km s^{-1} . The density contrast is proportional to the height of the surface above (or below) the plane of the plot (Hudson et al., 1995).

Princeton meeting *Critical Dialogues in Cosmology* between Burstein and Dekel, White acting as moderator (Dekel et al., 1997). The upshot of these considerations was that there was agreement that the value of Ω_0 is greater than 0.1 and a value of 0.2 to 0.3 would be consistent with most of the data.

The infall test became feasible on very large scales following the completion of the Two-Degree Field (2dF) survey of galaxy redshifts carried out at the Anglo-Australian Telescope. The survey involved measuring redshifts for almost 200,000 galaxies randomly selected from the Cambridge APM galaxy survey. A cut from that survey was shown in Fig. 2.8a. The concept behind the test was that that superclusters of galaxies generate a systematic infall of other galaxies in their vicinities and this would be evident in the pattern of recessional velocities, resulting in anisotropy in the inferred spatial clustering of galaxies. Using the redshifts of more than 141,000 galaxies from the 2dF galaxy redshift survey, Peacock and his colleagues discovered convincing statistical evidence for infall and estimated the overall density parameter to be $\Omega_0^{0.6} = 0.43b \pm 0.07$, where b is the bias parameter, the factor by which visible matter is more clustered than the dominant dark matter. When this result was combined with data on the anisotropy of the Cosmic Microwave Background, their result favoured a low density Universe with $\Omega_0 \approx 0.3$ (Peacock et al., 2001).

When taken in conjunction with the results derived from the power spectrum of fluctuations in the Cosmic Microwave Background Radiation discussed in Sect. 15.9, the consensus view is that the best estimate of the overall density parameter for the Universe is $\Omega_0 \approx 0.25 - 0.3$. An immediate consequence of this result is that most of the mass in the Universe cannot be in baryonic matter, which is constrained by the production of the light elements in the early stages of the Big Bang. As will be discussed in Sect. 10.4, the best estimate of the density parameter in baryons is $\Omega_{\text{bar}} = (0.0223 \pm 0.002)h^{-2}$, consistent with the results of analyses of the power spectrum of fluctuations in the Cosmic Microwave Background Radiation. Adopting $h = 0.7$, $\Omega_{\text{bar}} = 0.0455$ and so there cannot be sufficient baryons to account for

On scales greater than those of clusters of galaxies, estimates of the mass density in the general field can be found from the *cosmic virial theorem* (Peebles, 1976). In this procedure, the random velocities of galaxies with respect to the mean Hubble flow are compared with the varying component of the gravitational acceleration due to large-scale inhomogeneities in the distribution of galaxies. As in the other methods of mass determination, the mass density is found by comparing the random kinetic energy of galaxies with their gravitational potential energy, this comparison being carried out in terms of two-point correlation functions for both the velocities and positions of galaxies selected from the general field. Application to the random velocities of field galaxies suggested that Ω_0 might be larger than 0.2 (Davis et al., 1978; Davis and Peebles, 1983).

A similar argument involves studies of the infall of galaxies into superclusters of galaxies. Galaxies in the vicinity of a supercluster are accelerated towards it, thus providing a measure of the mean density of gravitating matter within the system. The velocities induced by large-scale density perturbations depend upon the density contrast $\delta\varrho/\varrho$ between the system studied and the mean background density. A typical formula for the infall velocity u of test particles into a density perturbation is (Gunn, 1978):

$$u \propto H_0 r \Omega_0^{0.6} \left(\frac{\delta\varrho}{\varrho} \right)_0 \quad (8.33)$$

In Gunn's analysis, this method resulted in values of Ω_0 about 0.2 to 0.3. In the case of small spherical perturbations, a result correct to second order in the density perturbation was presented by Lightman and Schechter (Lightman and Schechter, 1990).

$$\frac{\delta v}{v} = -\frac{1}{3} \Omega_0^{4/7} \left(\frac{\delta\varrho}{\varrho} \right)_0 + \frac{4}{63} \Omega_0^{13/21} \left(\frac{\delta\varrho}{\varrho} \right)_0^2 \quad (8.34)$$

In an ambitious programme, Dekel and his colleagues devised numerical procedures for deriving the distribution of mass in the local Universe entirely from the measured velocities and distances of complete samples of nearby galaxies, the objective being to determine a three-dimensional map of velocity deviations from the mean Hubble flow. Then, applying Poisson's equation, the mass distribution responsible for the observed peculiar velocity distribution can be reconstructed numerically. Figure 8.12 shows an example of a reconstruction of the local density distribution using this procedure (Hudson et al., 1995). Despite using only the velocities and distances, and *not* their number densities, many of the familiar features of our local Universe are recovered – the Virgo supercluster and the ‘Great Attractor’ can be seen as well as voids in the mean mass distribution. These procedures tended to produce somewhat larger values of Ω_0 , Dekel stating that the density parameter is greater than 0.3 at the 95% confidence level.

The issue of the total amount of dark matter present in the Universe was the subject of heated debate throughout the 1990s. Some flavour of the points of contention among the experts in the field can be gained from the discussions at the 1996

the observed total mass density. Most of the mass in the Universe must be in some non-baryonic form.

8.8 Summary

From a subject dogged by controversy and strong feeling for most of the twentieth century, classical cosmology saw a dramatic change in perspective during the last decade. New methods were developed which eliminated many of the problems of the pioneering efforts of previous decades. Whilst the emphasis in this chapter has been upon the traditional route to the determination of cosmological parameters, the consensus picture received a remarkable boost from analyses of the fluctuation spectrum of the Cosmic Microwave Background Radiation, a story which is told in the context of the understanding of the formation of large-scale structures in the Universe in Chap. 15. Indeed, many cosmologists would now look first to these observations as providing the key to unlocking many of the problems of the determination of cosmological parameters.

9 The Thermal History of the Universe

We are now well on our way to setting the scene for our attack on the problems of understanding the origin and evolution of galaxies and the large-scale structure of our Universe. Before we can do that, however, we need to work out in some detail the thermal history of the matter and radiation content of the Universe according to the standard Big Bang picture. In this chapter and Chap. 10, we develop a number of concepts which are essential for understanding the problems of galaxy formation. We first consider the dynamics of radiation-dominated universes.

9.1 Radiation-Dominated Universes

For a gas of photons, massless particles or a relativistic gas in the ultrarelativistic limit $E \gg mc^2$, pressure p is related to energy density ε by $p = \frac{1}{3}\varepsilon$ and the inertial mass density of the radiation Q_r is related to its energy density ε by $\varepsilon = Q_r c^2$. If $N(\nu)$ is the number density of photons of energy $h\nu$, then the energy density of radiation is found by summing over all frequencies

$$\varepsilon = \sum_{\nu} h\nu N(\nu). \quad (9.1)$$

If the number of photons is conserved, their number density varies with scale factor a as $N = N_0 a^{-3} = N_0 (1+z)^3$ and the energy of each photon changes with redshift by the usual redshift factor $\nu = \nu_0 (1+z)$. Therefore, the variation of the energy density of radiation with redshift is

$$\varepsilon = \sum_{\nu_0} h \nu_0 N_0 (\nu_0) (1+z)^4 = \varepsilon_0 (1+z)^4 = \varepsilon_0 a^{-4}. \quad (9.2)$$